




# Dynamic mechanical characteristics of an artificial porous granite under various water saturation levels

Ying Xu<sup>1</sup> · Songshan Lin<sup>1</sup> · Liyuan Jiang<sup>1</sup> · ShuaiShuai Ma<sup>1</sup> · Yan Fu<sup>1</sup> · Bangbiao Wu<sup>1</sup> 

Received: 17 January 2023 / Accepted: 12 November 2023 / Published online: 23 December 2023  
© Springer-Verlag GmbH Germany, part of Springer Nature 2023

## Abstract

Water content plays a significant role in the dynamic mechanical properties of rocks in hydraulic, deep underground, and mining engineering. However, the previous study generally concentrated on the oven-dried and water-saturated rock with spherical pores. Therefore, this study aims to investigate the impact of different water saturation levels and microstructure on the dynamic mechanical properties of artificial porous rock (APR) with multi cracks. The specimens with six water saturation levels (100%, 80%, 60%, 40%, 20%, and 0%) were tested under various loading rates using a split Hopkinson pressure bar (SHPB). The obtained results include the typical failure modes, stress–strain curves, dynamic uniaxial compressive strength (DUCS), fragmentation performance, and energy dissipation. The findings indicate that the DUCSs of unsaturated specimens initially increase with water saturation (20% ~ 80%) but subsequently decrease to the lowest value under fully saturated conditions. The dissipated energies of wet specimens are higher than that of dry specimens. Moreover, the dry specimen is prone to fail in a rock burst pattern, whereas the wet specimens exhibit a pulverization pattern. In addition, the corresponding water-effect mechanisms are discussed based on the microstructure of the APR.

**Keywords** Water saturation · Artificial porous rock · Microstructure · Loading rates · SHPB

## Introduction

In the fields of hydraulic, deep underground, and mining engineering, fissures in rocks provide storage spaces for free water (Wasantha et al. 2018; Zhang and Gao 2015). Water presence has dual effects on the mechanical properties of rocks. On the one hand, it can weaken the mechanical properties of rocks (Hawkins and McConnell 1992; Vasarhelyi and Van 2006; Wong et al. 2016), causing geological hazards (Erguler and Ulusay 2009; Zhang and Gao 2015; Zhao et al. 2021) and promoting rock breakage (Zhou et al. 2018). On the other hand, water enhances rock strength, especially under high loading rates (Zhao et al. 2022; Zhou et al. 2016). This property is widely adopted to mitigate rock bursts in practical engineering by spraying water or injecting water into the surrounding rocks (Gu et al. 2019). Therefore, it is imperative to investigate the influence of water on the

mechanical properties of rock materials to understand rock breakage and reduce the impact of natural disasters.

In engineering projects, rocks are frequently subjected to dynamic loadings due to explosions and impact loads (Sheng et al. 2019; Xia and Yao 2015). Several studies have investigated the dynamic behaviors of rock under the influence of water saturation, including dynamic compressive strength (Kim and Changani 2016; Ma et al. 2020; Zhou et al. 2016), fragment type (Cai et al. 2020a; Gu et al. 2019), and various energies during loading processes (Cai et al. 2020a; Gu et al. 2019). Most of them performed experiments on either oven-dried or fully-saturated rocks. However, rock materials are usually unsaturated in practical engineering applications. Therefore, it is significant to investigate the dynamic mechanical properties of rocks under different water saturation levels. Furthermore, examining the mechanical properties of multi-unsaturated specimens is beneficial for exploring the mechanism of the water effect.

Several mechanisms have been proposed to explain the effect of water saturation on mechanical characteristics of rocks. These mechanisms can be classified into physical, chemical, and mechanical ones. Physical mechanisms include changes in surface energy (da Silva et al. 2008; Zhou

✉ Bangbiao Wu  
bbwu@tju.edu.cn

<sup>1</sup> State Key Laboratory of Hydraulic Engineering Intelligent Construction and Operation, Tianjin University, Tianjin 300072, China

et al. 2018) and swelling of the material (Einstein 1996; Erguler and Ulusay 2009). Chemical mechanisms are usually related to the hydrolysis of quartz (Atkinson 1982; Hadizadeh and Law 1991) and potassium feldspar (Gang 2003), which are the two primary mineralogical compositions in granite. Mechanical mechanisms, such as the pore pressure effect (da Silva et al. 2008; Van Eeckhout 1976), subcritical crack growth (Kranz 1979; Tang 2018), Newton's inner friction effect (Daugherty and Franzini 1965; Wang et al. 2009), Stefan effect (Rossi 1991; Zhao et al. 2016), and meniscus effect (Daugherty and Franzini 1965; Wang et al. 2009), seem to be more abundant. Moreover, Wang et al. (2020) analyzed the interaction in water-saturated sandstones using an ideal model of two particles. Gu et al. (2019) proposed a similar diagram for soft coal to determine its micromechanical mechanism. Notably, these studies have concentrated on sedimentary rocks with natural spherical pores. However, inherent defects in rocks are both in the form of spherical pores and cracks. Studies on the effect of water saturation on the mechanical properties of multi-crack-type rocks are still scarce. A study has demonstrated that microstructure significantly affects the dynamic mechanical properties of rocks (Xia et al. 2008). The effects of water saturation on dynamic mechanical properties are also highly variable owing to microstructural features (Dyke and Dobereiner 1991; Ma et al. 2020; Wasantha et al. 2018). By exploring the water effect mechanism of multi-crack rocks, the microstructural role of the mechanism can be further elucidated.

This study primarily investigated the water saturation effect on the dynamic compressive characteristics of clay-free rocks with multi microcracks. By comparing with sedimentary rocks, whose microstructures primarily includes spherical pores, the role of the microstructure in determining the effect of water saturation on the mechanical properties of the rocks could be investigated. An artificial porous rock (APR), primarily containing cracks, was selected in this study as a clay-free specimen. Impact experiments on APR

specimens with 0%, 20%, 40%, 60%, 80%, and 100% water saturations under different loading rates were conducted using a modified split Hopkinson pressure bar (SHPB) system. The dynamic uniaxial compressive strengths and energy consumption of the specimens were investigated to determine the water saturation effect on the mechanical behavior of the specimens. Subsequently, fragments of the specimens were collected and analyzed to determine the fragmentation types and compare the fragment size distribution.

## Specimen preparation and experimental methodology

### Material characterization

Isotropic and homogeneous granite from the Fangshan District in Beijing, China, was selected to prepare the APR specimen. Fangshan granite (FG) is a medium-grained intrusive plutonic rock with mineral components such as plagioclase (Pl, 40%), potassium feldspar (Kfs, 35%), quartz (Qtz, 20%), and biotite (Bt, 5%). The average original porosity of FG is about 0.43%. All the specimens were prepared according to the International Society of Rock Mechanics and Rock Engineering (ISRM) method (Zhou et al. 2012). First, FG cores with a nominal diameter of 50 mm were drilled from the same block with the same orientation. Then, the cores were sliced into discs with an average thickness of 25 mm, that is, the length–diameter ratio was 0.5 (Fig. 1a). The end surfaces of the disc FG specimens were polished to achieve flatness within 0.25 mm and a parallelism of 0.25° to meet the requirement of the method suggested by ISRM (Zhou et al. 2012).

Figure 1b shows the microstructure of FG under cross-polarized light. To increase the porosity of the APR specimens, the FG specimens were heat-treated at 1000 °C, which is the most optimal temperature determined in the

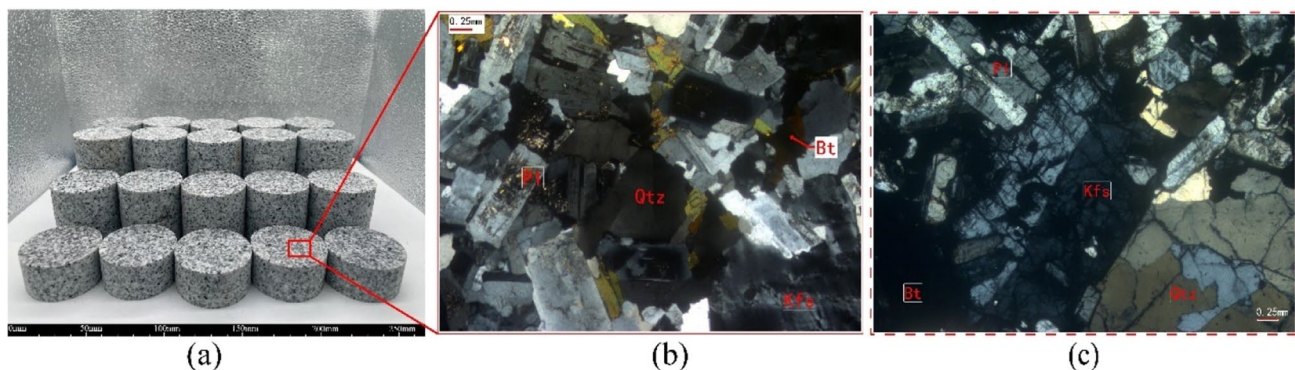


**Fig. 1** Fangshan granite (FG) specimen: **a** original FG specimens, **b** cross-polarization light (CPL) of FG, **c** polarized light micrographs of APR. Bt—Biotite; Qtz—quartz; Kfs—plagioclase; Pl—feldspar

literature (Jiang et al. 2021). By using an optical microscope with a magnification ratio of 50, a microscopic image of the APR was obtained as shown in Fig. 1c. This figure reveals numerous microcracks across the specimens, accounting for the high porosity of the APR. In addition, the cracks induced by heat treatment were evenly distributed throughout the specimens, as shown by computerized tomography images in the previous study (Jiang et al. 2021). Following the heat treatment at 1000 °C, the final porosity of the APR specimen was 5.83%, with a corresponding density of 2.53 g/cm<sup>3</sup>.

Figure 2 shows the relationship between the pore throat radius ( $\mu\text{m}$ ) and the corresponding distribution frequency, indicating that the pore space of the APR specimen is crack-dominant with small amounts of spheroidal pores. In addition, the permeability of the APR specimen is  $25.52 \times 10^{-15} \text{ m}^2$ , which can be considered a relatively high permeability ( $> 10^{-19} \text{ m}^2$ ) (Davy et al. 2007; Hu et al. 2010; Li and Liu 2021).

Subsequently, dry APR specimens were immersed in distilled water within an airtight container maintained in a vacuum environment for 48 h to obtain saturated specimens. The saturated specimens were dried to the desired water content in an oven according to the relationship between the saturation level and drying time (Jiang et al. 2021). Six groups of rock specimens with different water saturation levels (0%, 20%, 40%, 60%, 80%, and 100%) were prepared for the dynamic experiments. The physical and mechanical parameters of APR with various water saturation levels are summarized in Table 1 and Fig. 3.

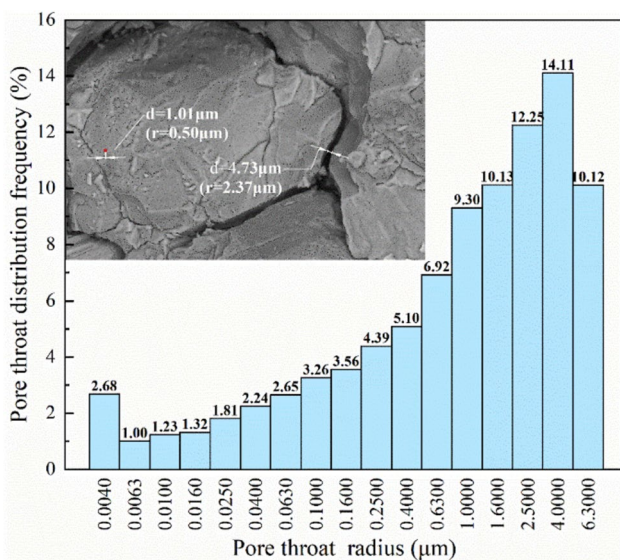


Fig. 2 Relationship between pore throat radius and pore throat distribution frequency

Table 1 Mechanical properties of the APR specimen with different water saturation levels

Saturation (%)	P-wave velocity (m/s)	Uniaxial compressive strength (MPa)	Elastic modulus (GPa)	Poisson's ratio
0	546.76	52.25	26.10	0.24
20	569.62	57.04	60.93	0.24
40	573.79	59.37	37.29	0.28
60	621.97	60.57	39.80	0.25
80	723.58	42.17	32.16	0.29
100	1509.80	40.39	57.35	0.19

### Experimental apparatus

The SHPB system has been suggested by the ISRM as a standard facility for investigating the dynamic properties of rock materials (Zhou et al. 2012). Currently, the mechanical behaviors of rocklike materials at intermediate and high strain rates ( $10^2\text{--}10^4 \text{ s}^{-1}$ ) have extensively been investigated using the SHPB system (Chen and Song 2011; Xia and Yao 2015; Zhang and Zhao 2014; Zhou et al. 2012). Thus, in this study, dynamic forces were loaded using a traditional SHPB system combined with a momentum trap (Wang et al. 2021). As shown in Fig. 4, the lengths of the strike, incident, transmitted, and absorption bars were 485, 3000, 1800, and 500 mm, respectively. All the bars are made of 7075 aluminum with a diameter of 50 mm, and the specific material parameters of the bars are listed in Table 2. When the striker is launched and impacts on the incident bar, a one-dimensional compressive stress wave (incident wave) is generated and propagates along the incident bar. When it reaches the interface between the incident bar and the specimen, part of it travels through

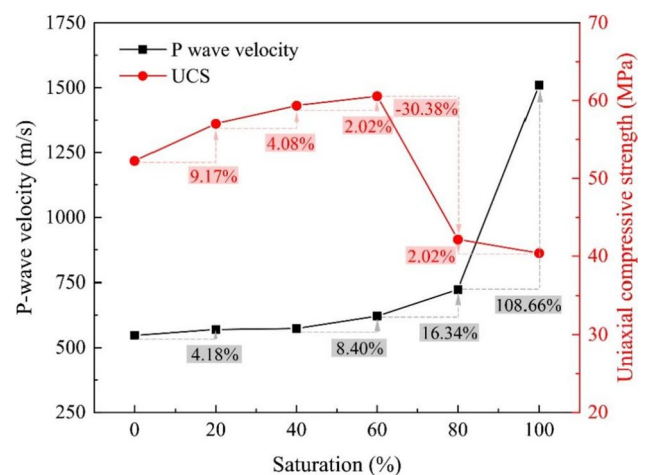


Fig. 3 P-wave velocity, UCS of the APR specimen under various saturation

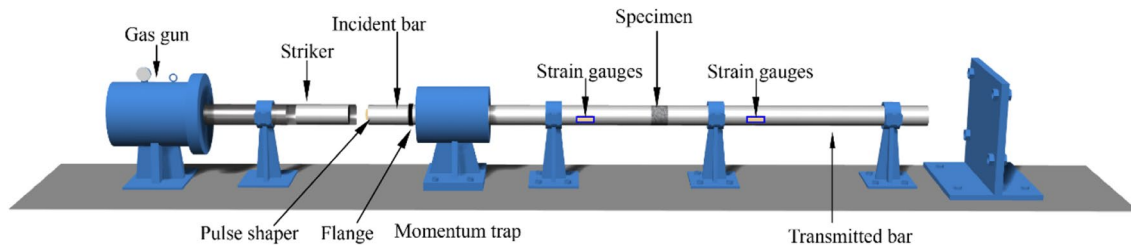


Fig. 4 Scheme of the SHPB testing system

Table 2 Material parameters of the bars

Density (g•cm <sup>-3</sup> )	Young's modulus (GPa)	Nominal yield strength (MPa)	P-wave velocity (m/s)
2.81	70	455	5050

the specimen and into the transmitted bar which is called the transmitted wave. Part of it is reflected as the reflected wave traveling back to the incident bar. Strain gages placed on the bars would measure the strains caused by the waves. In addition, to minimize wave dispersion, facilitate stress equilibrium, and maintain constant strain rate deformation (Chen and Song 2011), a pulse shaping technique is adopted using pulse shapers. Based on multiple experiments, the  $\phi$  22–24-mm disc with 3.0–5.0-mm thickness made of black rubber was sandwiched between the strike and incident bars to obtain an incident pulse with better profiles (Chen and Song 2011; Chen et al. 2003; Zhao et al. 2022).

The SHPB technology adopts two basic hypotheses: the one-dimensional stress wave theory and homogeneity assumption (Chen and Song 2011). The frontier is supported when the incident and transmission bars are sufficiently long with a relatively small diameter. The latter refers to stress, and strain is uniformly distributed along the axial direction of the specimen. In this way, according to the superposition principle of linear elastic waves, the loading stresses on the two ends of the FG specimen are

$$\sigma_1(t) = \sigma_i(t) + \sigma_r(t) = E(\epsilon_i(t) + \epsilon_r(t)) \tag{1}$$

$$\sigma_2(t) = \sigma_t(t) = E\epsilon_t(t) \tag{2}$$

where  $t$  is the time, and  $E$  is Young's modulus of the bars.  $\sigma_1$  is the incident end, and  $\sigma_2$  is the transmitted end. By using the above-mentioned pulse-shaping technique, the dynamic stress equilibrium can be obtained as  $\sigma_1 = \sigma_2$ . The dynamic stress equilibrium in a typical test is shown in Fig. 5. Therefore, the compressive stress of the APR specimen can be obtained as

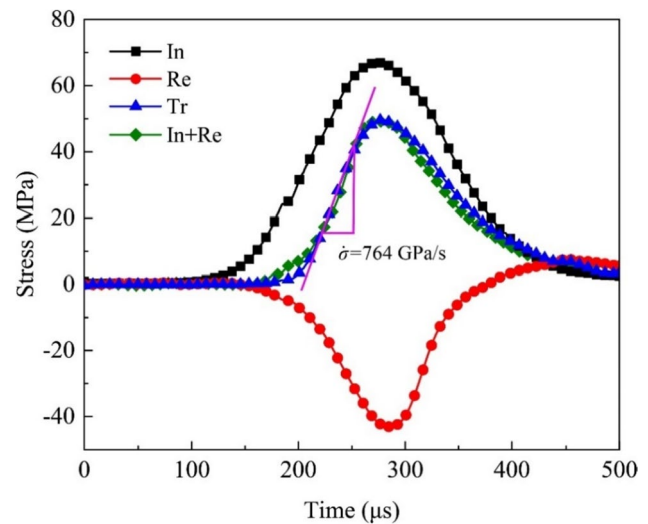


Fig. 5 Stress equilibration and determination of loading rate (In-incident stress, Re- reflected stress, and Tr-transmitted stress)

$$\sigma_c(t) = (\sigma_1(t) + \sigma_2(t)) \times A_b / 2A_s = A_b \sigma_1(t) / A_s \tag{3}$$

where  $A_b$  and  $A_s$  are the cross-sectional area of the bars (50 mm) and the diameter of the specimens (50 mm), respectively. The corresponding loading rates, calculated as the slope of the straight line in the loading process, are also obtained according to the suggested method of ISRM (Zhou et al. 2012), as shown in Fig. 5.

## Dynamic compression experimental results

### Axial stress–strain response

Figure 6 shows the axial stress–strain relationships of the APR specimens with different water saturation levels subjected to dynamic loading. Generally, the stress–strain curve of APR can be categorized into five stages: crack closure, elastic deformation, stable crack propagation, instability propagation, and post-peak stages. Under a certain water saturation level, as the loading rate increase, the peak compressive stress

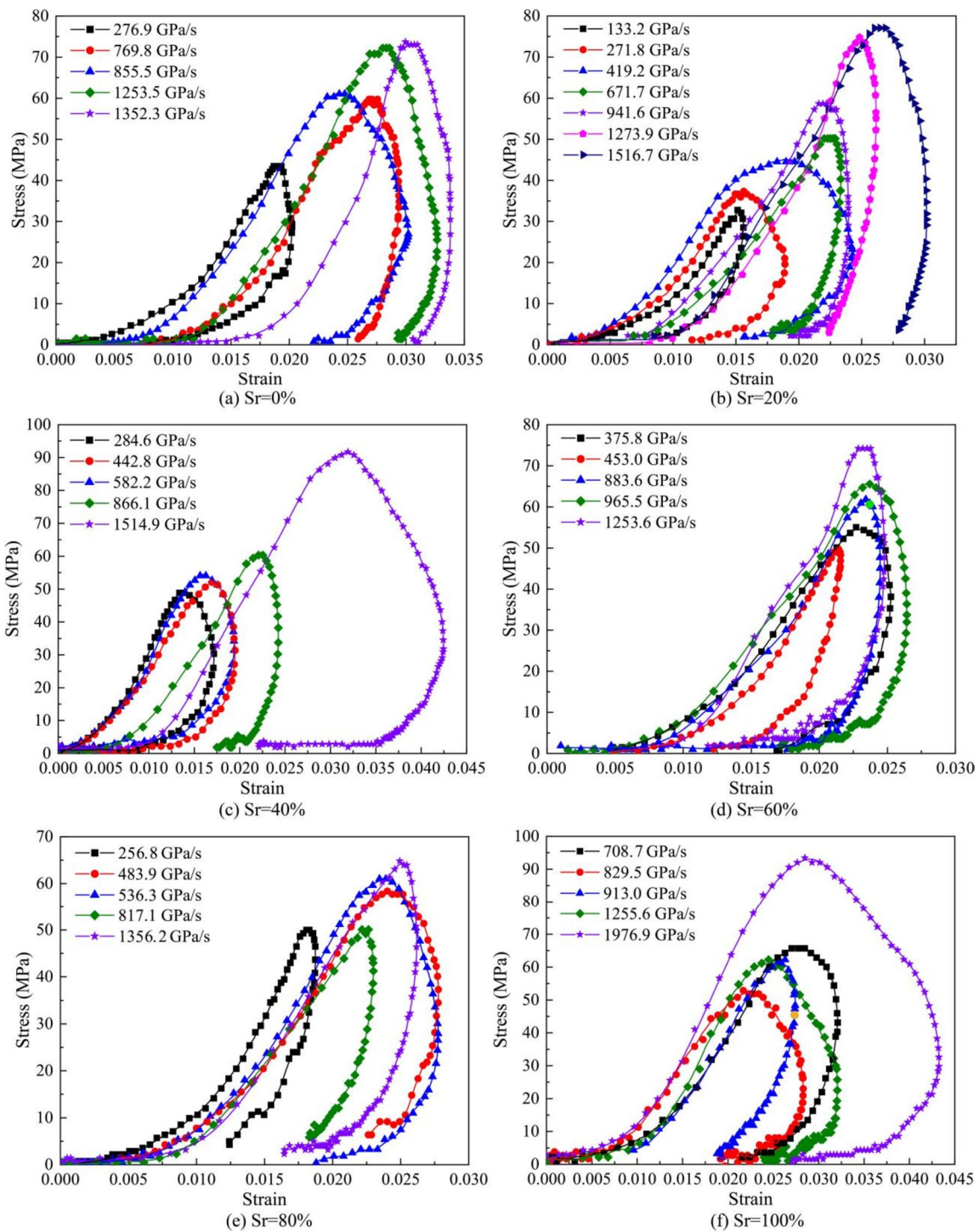


**Fig. 6** Strain–stress curves under various strain rates with certain water saturation levels

increased, accompanied by more intense fragmentation. Correspondingly, the peak strain exhibited similar relationship.

In the first stage (known as crack closure), as the water saturation level rises, the initial pore compaction phase extends its duration, by comparing the stress–strain curves of the specimens subjected to varying water conditions. This

may be attributed to the generation of a weakening area in the specimen at a microscopic level during the water saturation process, leading to a greater strain. In the second stage (elastic deformation), the slope of the stress–strain curve for the unsaturated specimen is slightly lower than that of the completely dry specimen, indicating that the unsaturated

specimen exhibits more plastic behavior. Consequently, the presence of pore water reduces the overall elasticity of the specimen. In the post-peak stage, the curve is hooked because the fragmentation of the specimen is not significant. This is a result of insufficient energy input rather than intrinsic slip weakening of rocks (Wawersik and Fairhurst 1970). The recovery of elasticity during this stage is a result of the unloading process, while partial fragmentation occurs due to the tensile wave reflected from the free surface of the specimens (Li et al. 2018). Moreover, certain stress–strain curves are not sufficiently smooth, particularly those of the completely dry specimens. This is probably owing to the abrupt change in the local stress due to the occurrence of multiple cracks and pores in the dry specimen. Therefore, the curve exhibits local concavity macroscopically.

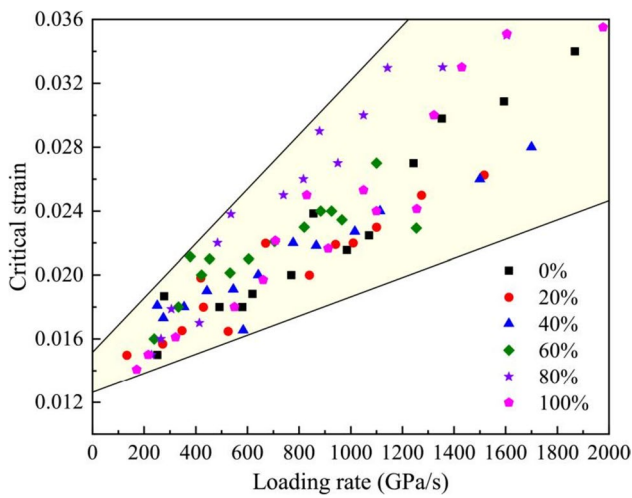


Fig. 7 Critical strain versus loading rates under various water saturation levels

To investigate the effect of water on the deformation of the APR specimens, the critical strains of the specimens are plotted, as shown in Fig. 7. The critical strain varies from 0.014 to 0.036. Generally, with an increase in water saturation levels, the critical strain exhibits an upward trend. Notably, the 80% saturated specimen exhibited the largest failure strain, whereas the 20% saturation exhibits the lowest failure strain. While the difference in critical strain between specimens with different water contents slightly increased with the loading rate, the difference remained relatively small. Nevertheless, it is evident that the loading rate influences the water saturation effect on the deformation of the specimens.

### Dynamic uniaxial compressive strength

The correlation between the dynamic uniaxial compressive strength (DUSC) and the loading rate of the APR specimens with various water saturation levels is shown in Fig. 8. It is obvious that the DUSCs of the APR specimens for all water saturation levels increased with the loading rate. Hence, the DUSCs of the APR specimens with various saturations exhibited rate dependence. To describe the effect of the loading rate and saturation, the following formula is proposed:

$$\sigma_{dc} = \left( 1 + \alpha \frac{\dot{\sigma}}{\dot{\sigma}_0} \right) \sigma_0 \quad (4)$$

where  $\sigma_{dc}$  is the DUSC,  $\dot{\sigma}$  is the loading rate,  $\dot{\sigma}_0$  ( $= 1 \text{ GPa/s}$ ) is the reference loading rate,  $\sigma_0$  is the compressive strength when the loading rate is approximately 0 GPa/s, and  $\alpha$  is the fitting parameter indicating rate dependence. The fitting curves and fitting parameters are shown in Fig. 8 and Table 3, indicating that the value of  $\alpha$  for the wet specimens is larger than that for the dry specimens. This phenomenon

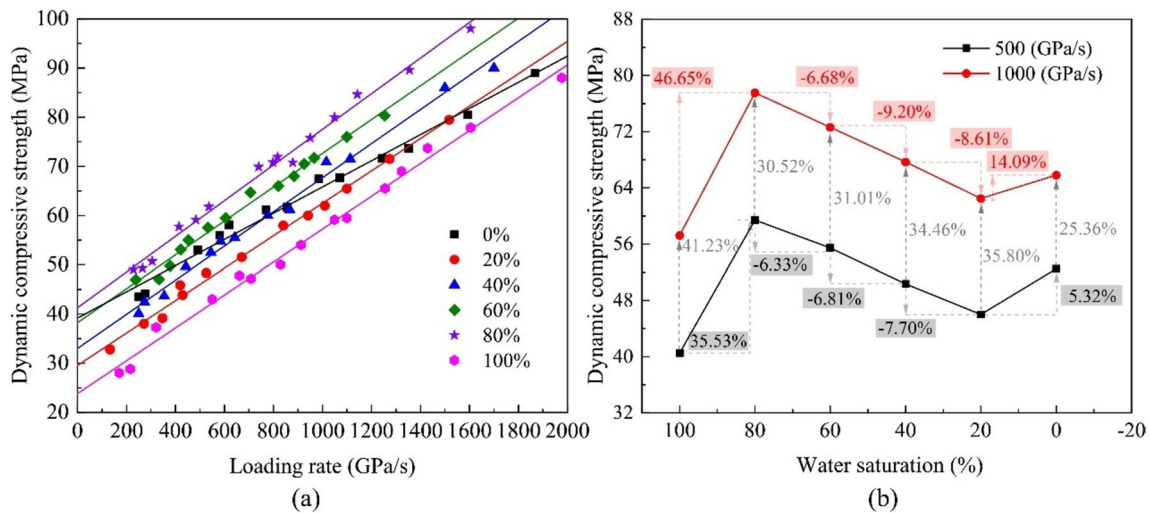


Fig. 8 Variation in the dynamic compressive strength with the loading rate for six water saturation levels

**Table 3** Fitting parameters for different water saturation levels

Water saturation	$\alpha$ ( $10^{-4}$ )	$\sigma_0$	$R^2$
100%	14.03	23.81	0.98
80%	8.79	41.27	0.99
60%	8.99	38.25	0.99
40%	10.52	32.99	0.98
20%	11.15	29.54	0.99
0%	6.79	39.19	0.98

is also observed in porous red sandstone (Cai et al. 2020b). These results collectively suggest that the presence of water enhances the rate dependency.

Additionally, the impact of water saturation on the DUCSs of the APR specimens is explored focusing on two specific loading rates (500 and 1000 GPa/s), as depicted in Fig. 8b. These values are obtained from the fitting curves presented in Fig. 8a. The DUCSs exhibit a similar trend for both loading rates. Notably, the lowest DUCSs for both loading rates corresponded to 100% saturation. This observation aligns with findings in sandstones (Cai et al. 2020b; Xu et al. 2022) and is also evident in quasi-static conditions (Fig. 3). The weakening phenomenon under 100% saturation can be attributed to two primary mechanisms. (1) Water filled in the pores lacks sufficient time to be expelled from the specimen during dynamic loading, leading to increased pore water pressure and weakened DUCSs compared to the unsaturated specimens (Cai et al. 2020a; Zhao et al. 2022). (2) When the specimens are fully saturated, water fills the crack tips, thereby decreasing the friction between particles (Van Eeckhout 1976), weakening the strength of the grain boundary surface, and reducing the internal connections between particles (Zhang and Gao 2015; Zhou et al. 2019).

When the saturation level is 80%, the DUCSs exceed those of the full saturated (100%) and dry specimens (0%). This notable increase in strength can be attributed primarily to the evaporation of pore water, which enhances the adhesion between water and the specimen matrix. Consequently, the strengthening effect becomes more pronounced, typically including Stefan's (Rossi 1991; Zhao et al. 2016) and Newton's inner friction effects (Wang et al. 2009). However, the DUCSs decrease gradually as the water saturation decreases from 80 to 20%, and the DUCS reaches the lowest value at 20% saturation. Interestingly, when the saturation reaches 0%, a distinct increase in DUCS is observed for both loading rates. This indicates a change in the deformation behavior of the specimens in the absence of water, resulting in a different response to the applied dynamic loading. In addition, except for the 20% saturation, the DUCSs of unsaturated APR specimens are larger than those of dry ones. The enhancement mechanisms of pore water on the DUCSs are similar to those on

the UCSs of the APR specimens and other natural rock materials (Jiang et al. 2021; Zhou et al. 2016).

### Fragmentation analysis

A single loading technique was adopted using a momentum trap, which is also a prerequisite for conducting a valid quantitative fragmentation analysis. To ensure the accuracy of the study, all APR specimens with varying water saturation levels were recovered after tests using a transparent polymethyl methacrylate box (Wang et al. 2021). Recovered rock fragments for typical APR specimens are illustrated in Fig. 9. According to fragment characteristics (Cai et al. 2020a; Xia et al. 2008; Xu et al. 2020), failure patterns can be categorized into three types: cracked, rock burst, and pulverization patterns.

In terms of the cracked pattern (Fig. 9a), several visible cracks appear on the surface of the specimen. This type primarily occurs at lower loading rates (< 350 GPa/s in this study). Another failure pattern is that the specimens were split into strips (Fig. 9b), and the length of the primary strips was approximately the same as the thickness of the specimen, and the others were only locally slabbed or buckled from the free sides. This failure type is recognized as rock bursts (Cai et al. 2020a). In the pulverization pattern, the specimen was pulverized into smaller particles, with most of them having a diameter less than 10 mm, as shown in Fig. 9c (Cai et al. 2020a). The failure modes of the APR specimens under various loading rates and water saturation levels are summarized in Fig. 10. Notably, the wet specimen can more likely be pulverized, whereas the failure patterns of the dry specimens are predominantly rock bursts under the same loading condition until approximately 1000 GPa/s. This phenomenon shows the effect of water saturation in mitigating rock burst hazards in deep rock engineering. The required loading rate for pulverization failure increases with higher degrees of water saturation. In addition, microcracks with different lengths and morphologies were randomly distributed across the specimen. Consequently, even if the two specimens had the same water saturation at similar loading rates, their failure patterns were distinct due to these inherent differences in microcrack distribution.

Fragmentation analysis was performed using the manual sieving method on the fragmented rocks. It includes seven sieves with mesh sizes of 40, 20, 10, 5, 2, 1, 0.5, 0.25, and 0.075 mm. The sieves were stacked in descending order, and a container was placed at the bottom. Initially, the recovered fragments were placed on top of the sieve device. Then, the shattered fragments on each sieve were flicked slightly to select fragments with a certain diameter. Subsequently, the fragment mass in each sieve and the container was weighted, and the fragment size distribution (FSD) was obtained.

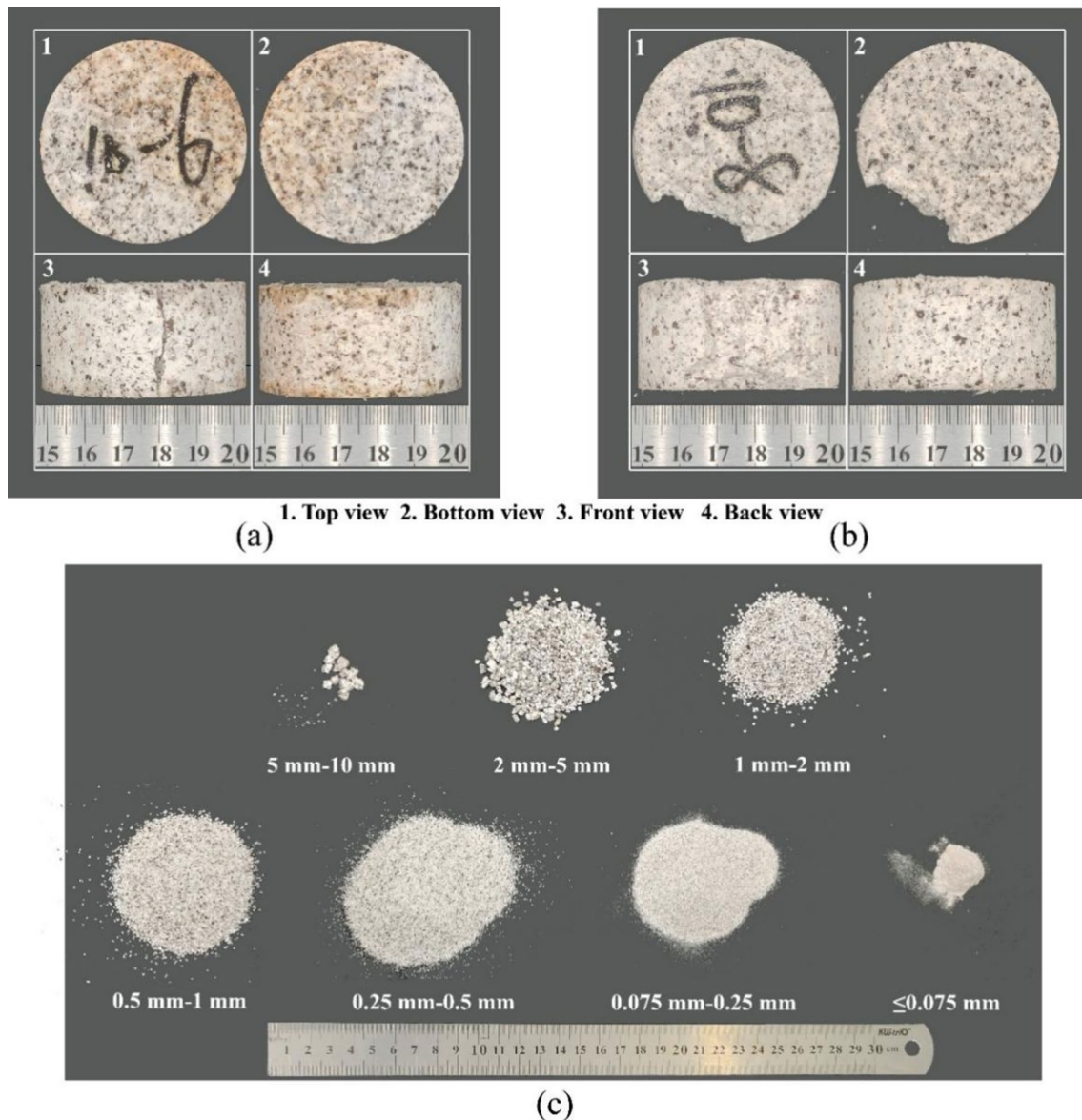


**Fig. 9** Three typical failure types: **a** cracked pattern; **b** rock bursts pattern; **c** pulverization pattern

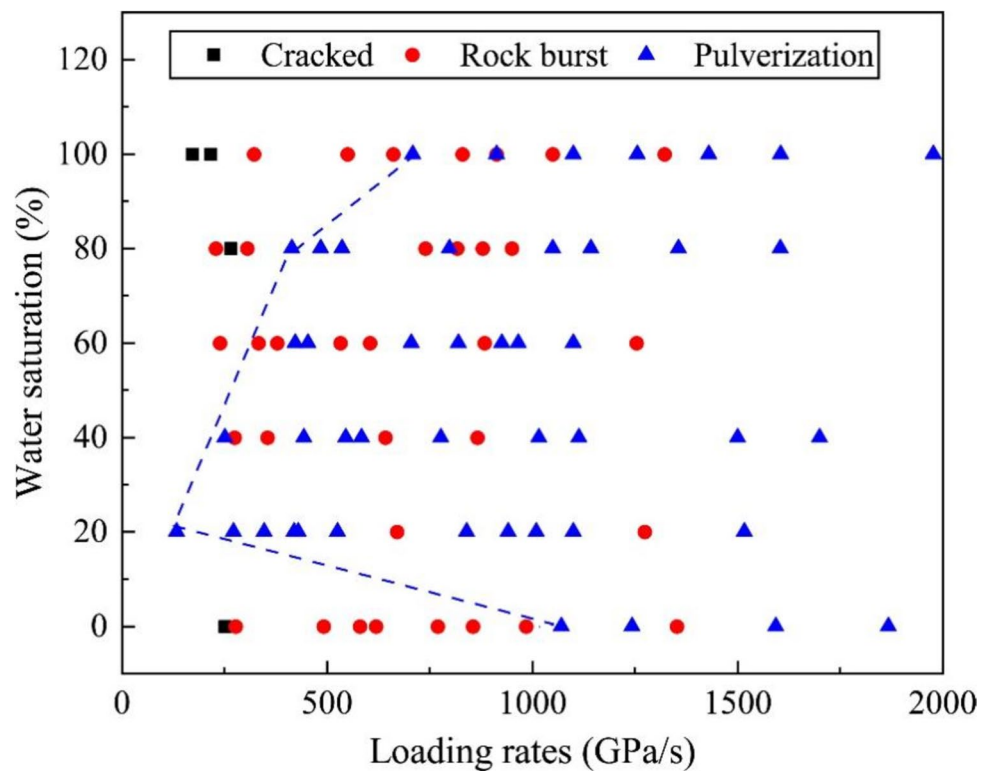
Noticeably, the mass loss of the specimen within 3% was considered valid.

The FSD curves of specimens with different water saturation levels at lower (< 350 GPa/s), medium (550–750 GPa/s), and higher (> 900 GPa/s) loading rates are shown in Figs. 11a, b, and c, respectively. To accurately reflect the fragment size distribution, the half-logarithm coordinate system was used for a relatively large fragment size range (Hong et al. 2009). Figure 11a shows that the APR specimens with water saturation levels of 0%, 80%, and 100% remain intact at lower loading rates, while those with 20% and 40% water saturation are pulverized into fine debris. This suggests that an APR specimen with low water saturation is prone to crushing within this loading rate range. Figure 11b reveals

that the dry specimen is less prone to crushing at medium loading rates (550–750 GPa/s) compared to the wet specimens, indicating that the presence of water exacerbates failure (Cai et al. 2020a; Gu et al. 2021). Notably, the difference in the particle size distributions among the wet specimens is smaller at lower loading rates (Fig. 11a), indicating that the loading rate limits the sensitivity of rock crushing to the water saturation degree. At a higher loading rate (Fig. 11c), the particle size distributions of all the specimens tend to be consistent, with pervasive pulverization observed in all cases. Additionally, the dry specimens exhibit greater pulverization compared to the wet specimens. Among the different water saturation levels, specimens at 20%, 40%, and 60% water saturation are crushed at all loading rate ranges,



**Fig. 10** Failure patterns of the APR specimens versus loading rates and water saturation degree



while others display greater sensitivity to loading rates, primarily failing at higher loading rates. Moreover, the fragmentation of the APR specimens of all the water saturation degrees exhibits an increasing trend with the loading rates, implying that the fragmentation of the APR specimens is more sensitive to the loading rate than the water saturation degree. The average fragment sizes (AFS) were calculated and summarized in Fig. 11d. It is interesting that all the AFSs of wet specimen are smaller than dry ones at the loading rate ranges in this study. Notably, the AFSs of specimens with water saturation levels 20%, 40% and 60% are lower than those of 80%, 100% and dry ones at all loading rate ranges. At higher loading rates (> 1000 GPa/s), the AFS of wet specimens tend to be consistent.

**Energy dissipation**

From a thermodynamic perspective, material failure is an unstable, energy-driven phenomenon. Hence, the effect of water on the energy dissipation during APR specimen failure should be investigated. According to the wave propagation theory, the total energy absorbed by a specimen is:

$$\Delta W = W_i - W_r - W_t \tag{5}$$

In this equation, the incident ( $W_i$ ), reflected ( $W_r$ ), and transmitted energies ( $W_t$ ) can be calculated as

$$W = A_0 C_0 \int E_0 \epsilon^2(t) dt \tag{6}$$

where  $A_0$ ,  $E_0$ ,  $C_0$  are the elastic modulus, cross-sectional area, and elastic wave velocity of the bars, respectively.

During dynamic tests, the absorbed energies primarily contribute to damaging the specimens (Barber and Griffith 2017). These energies include fracture energy (Xu et al. 2022), specimen deformation (Aben et al. 2017), kinetic energy (Xu et al. 2020), and other forms (e.g., heat, sound). For brittle rock materials undergoing dynamic compression tests, deformation and kinetic energy play a relatively minor role. The dissipated energy, which is essentially fracture energy in this context, is approximately equal to the absorbed energy  $\Delta W$ , and both are consumed in generating new surfaces. The dissipated energy of the APR specimens at various levels of water saturation and loading rates is shown in Fig. 12. It is evident that the dissipated energy increases with higher loading rates. However, the impact of water saturation on the dissipated energy remains limited.

To minimize the influence of the volume discrepancies of the specimens, the dissipated energy density, defined as the ratio of energy to the specimen volume, was selected as the reference. The relationships between the dissipated energy density, incident energy, failure pattern, and level of water saturation are depicted in Fig. 13. Notably, when the dissipated energy density is between 0.028 and 0.189 J/cm<sup>3</sup>, almost all the specimens exhibit cracked patterns as

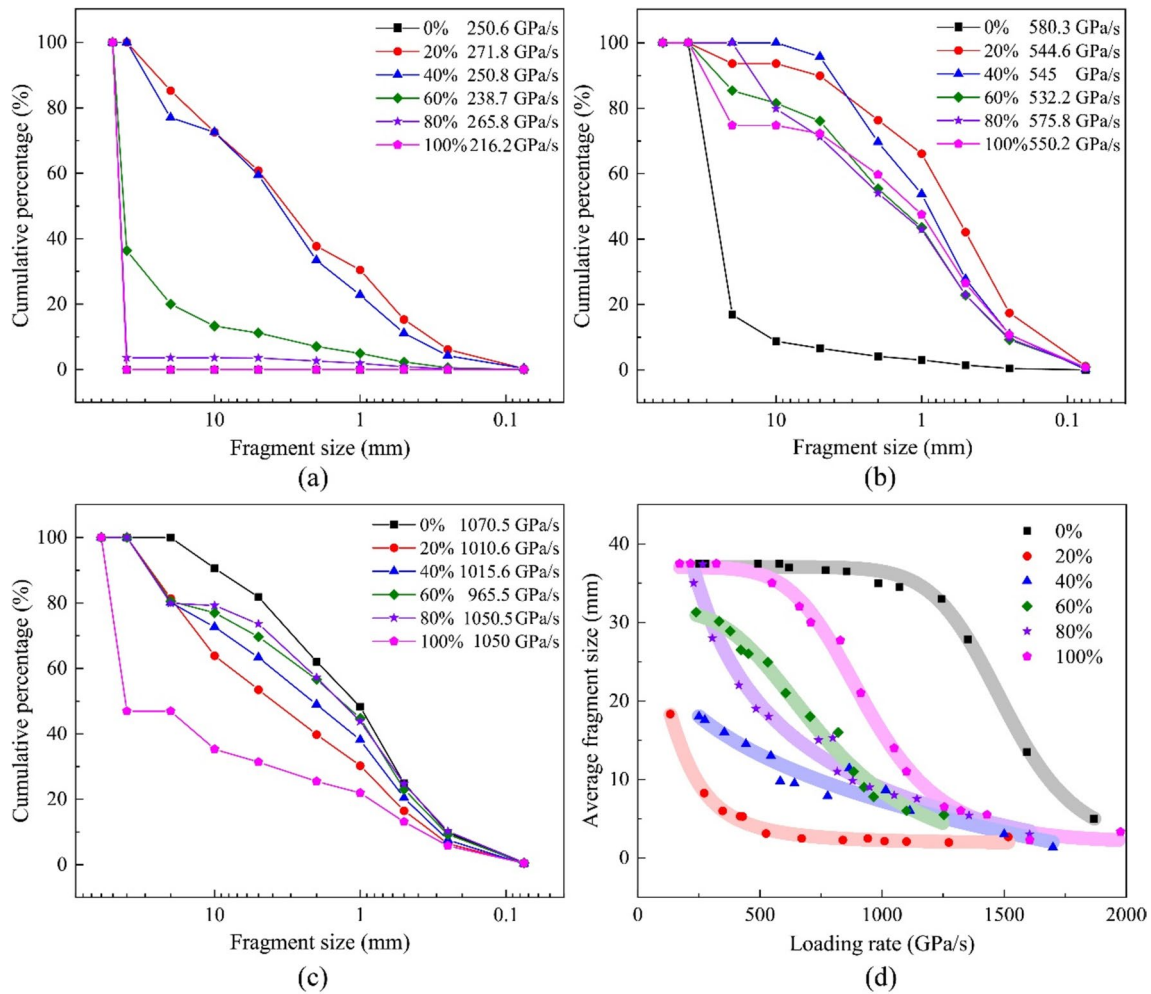


**Fig. 11** Fragment size distributions of APR specimens with different water contents at different loading rates: **a** ~ 250 GPa/s loading rate; **b** ~ 550 GPa/s loading rate; **c** 1000 GPa/s loading rate; **d** average fragment size vs. loading rate

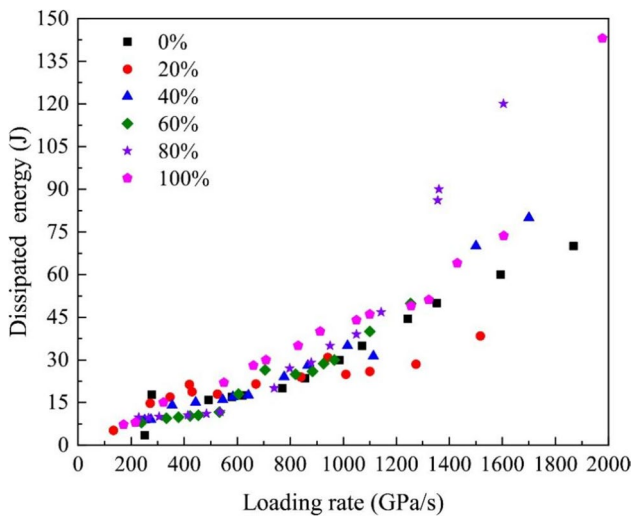
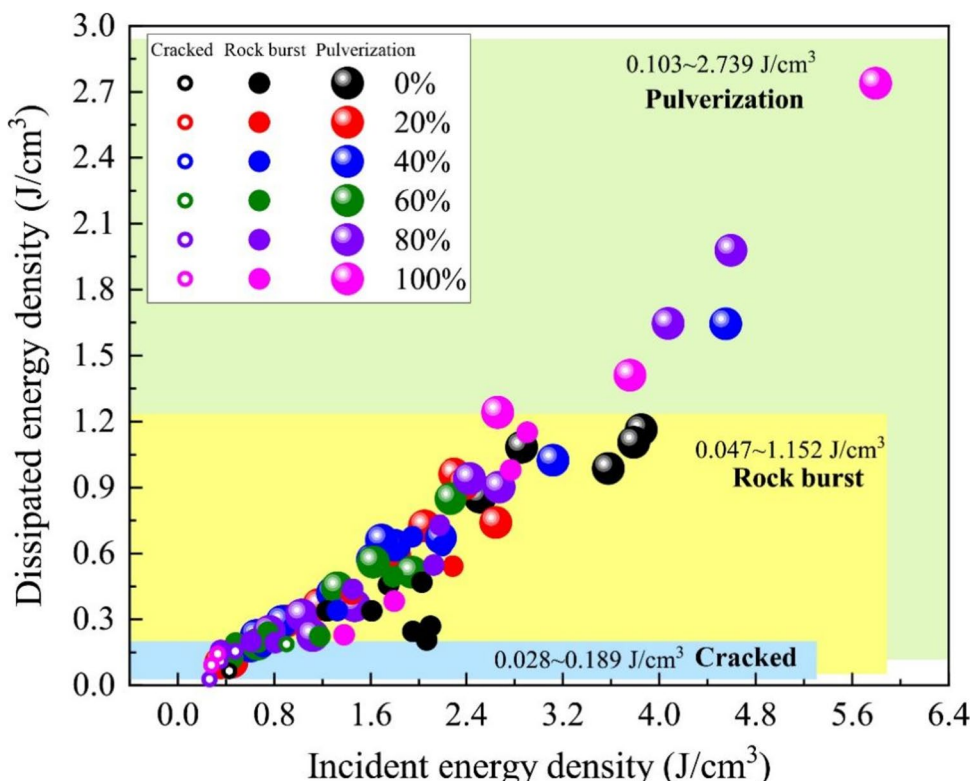


**Fig. 12** Relationship between loading rate and dissipated energy

the failure mode. With an increase in the incident energy density, the dissipated energy density required for specimen failure increases correspondingly, leading to failure patterns primarily consisting of rock bursts and pulverization. Notably, the required dissipated energy densities of rock burst and pulverization failures have overlapping regions, suggesting the randomness of the failure pattern in response to dynamic loading conditions.

Furthermore, the wet specimens required a statistically higher amount of dissipated energy for failure compared to the dry specimens at a given incident energy density. This indicates that the presence of pore water dissipated sufficient energy for generating new crack surfaces, and thus inducing finer particles. This phenomenon has also been observed in rock breakage and excavation construction studies (Abu Bakar and Gertsch 2013; Abu Bakar et al. 2014). Additionally, when the incident energy density is between 0.8 to 2.4 J/cm<sup>3</sup>, the dry specimens are more prone to fail in the rock burst pattern, while most of the wet specimens exhibit

**Fig. 13** Variation in the dissipated energy density with the incident energy density



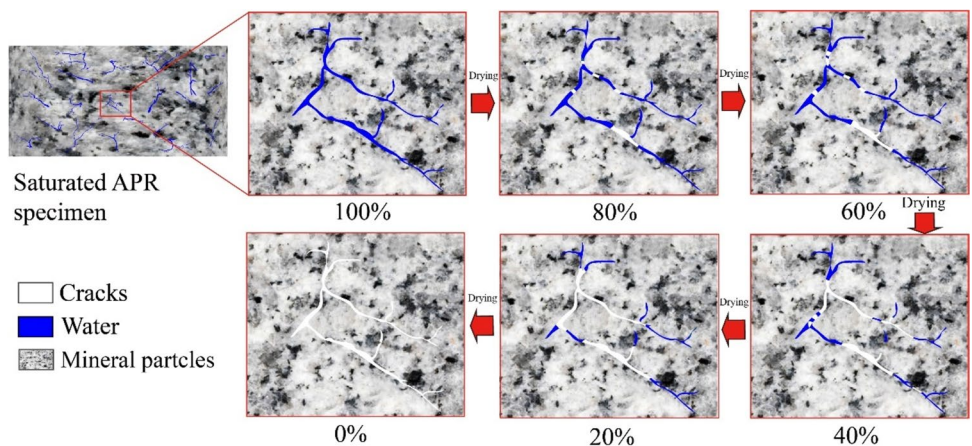
pulverization patterns. This finding provides further evidence that the application of water, either through spraying or injection, in the surrounding rocks of tunnels has a mitigating effect on rock burst disasters in practical engineering.

**Discussion**

Some studies have demonstrated that pore water has both weakening and strengthening effects on the strength of saturated rock materials, as observed in both static and dynamic experiments (Jiang et al. 2021; Masoumi et al. 2017; Zhou et al. 2016). Under static conditions (Fig. 3), the UCSs of

the APR specimens initially increase with saturation level, reaching the highest value at 60% saturation, and then gradually decrease with further saturation. This trend differs from that of the P-wave velocity, which gradually increases with higher saturation. This discrepancy indicates that with a decrease in water content (from 100 to 60%), air gradually replaces pore water. Consequently, this induces a sharp decrease in the P-wave velocity, while simultaneously, the Stefan effect comes into effect, resulting in an increase in UCS. As the saturation continues to decrease, the weakening effect prevails over the strengthening meniscus effect caused by the residual water at the crack tips (Fig. 14), ultimately leading to the reduction of UCS (Fig. 3).

**Fig. 14** Schematics of the APR specimens under different water saturation levels

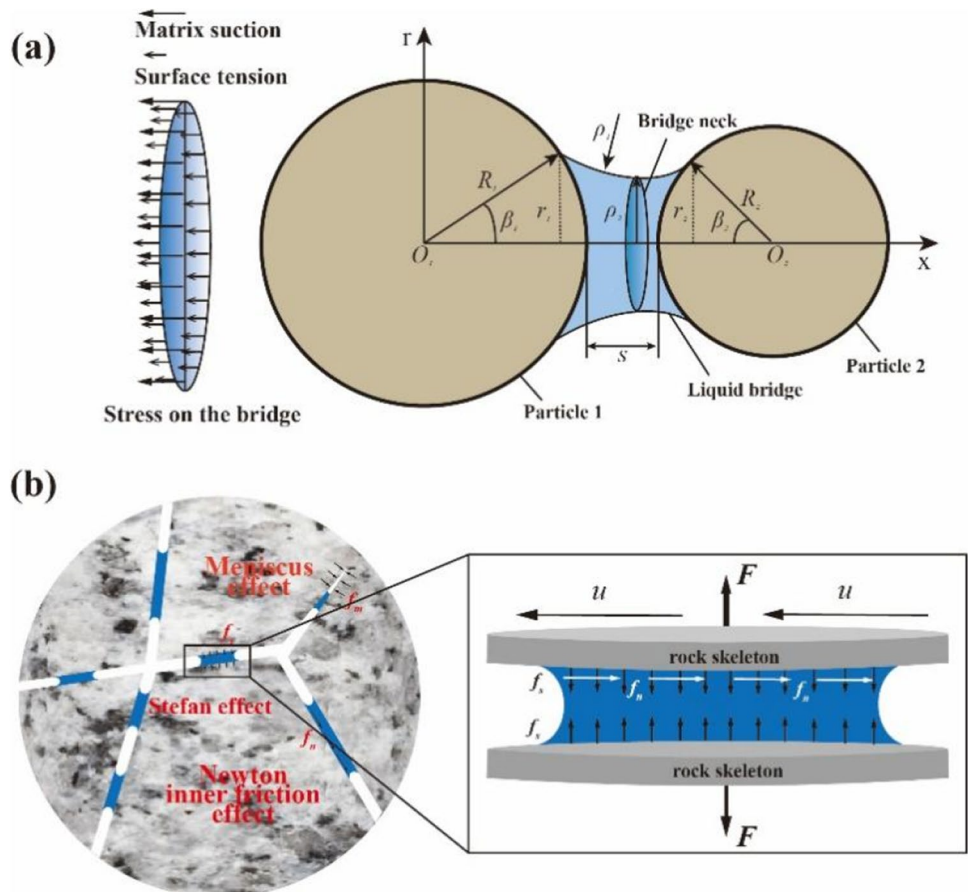


Unlike the case under quasi-static conditions, the residual water in the crack tips first weakens the DUCSs at 20% saturation under dynamic conditions (Fig. 8). This discrepancy is primarily due to the localized weakening of pore water on the rock's resistance to fracture during dynamic tests. Notably, the fragment size at 20% is the smallest at a given loading rate (Fig. 11). Subsequently, the DUCSs increase with the water saturation (from 20 to 60%). This trend is similar to the UCSs shown in Fig. 3. With increasing water content, multiple contact areas were involved between the rock matrix and pore water. The adhesion effect caused by the Stefan and Newton-inner friction effects becomes significant in the saturation level from 20 to 60%. When the saturation level is 80%, the DUCS reaches the highest value, while the UCS decreases and becomes lower than that of the dry specimens (Fig. 3). This indicates that the Stefan and Newton-inner friction effects outweigh the weakening effect owing to the shorter loading time in dynamic tests. When the pores and cracks are fully filled with water, the DUCSs drop to the lowest value, primarily because of the water wedging resulting from localized pore water pressure (Zhou et al. 2016), similar to the mechanism observed under quasi-static conditions (Huang et al. 2021; Jiang et al. 2021). In addition, in contrast to dry APR specimens, under dynamic

conditions, the presence of pore water around the crack tips promotes crack initiation and propagation in the wet APR specimens. This is consistent with the observed failure pattern, where the fragmentation of the wet specimens is finer than that of dry ones at a given loading rate (Fig. 11).

Microstructures of the specimens can be crucial to the mechanical behavior of rocks (Dyke and Dobereiner 1991; Ma et al. 2020; Sheng et al. 2019; Wasantha et al. 2018). Generally, the selected specimens were natural sedimentary rocks with spheroidal pores (Cai et al. 2020b; Gu et al. 2019; Sheng et al. 2019; Wang et al. 2020). Gu et al. (2019) and Wang et al. (2020) simplified the microstructure as two spherical particles to analyze the water effect mechanism. They stated that the pore water between the particles was in the form of a liquid bridge, as shown in Fig. 15a. The dynamic cohesive force between the particles consists of the attraction between the two particles and the liquid bridge force. Thus, capillary pressure and surface tension are key control factors for the mechanical behaviors of specimens (Gu et al. 2019; Wang et al. 2020). For the APR specimens, their microstructures are proposed as two plates, as shown in Fig. 15b. The narrow crack promotes the Newton inner friction ( $f_n$ ) and Stefan effects ( $f_s$ ). Thus, the water-strengthening effect on macro mechanical properties becomes noticeable

**Fig. 15** Two typical microstructures of (a) sedimentary rock and (b) APR



at water saturation from 20 to 80%. In addition, the meniscus effect at the crack tip is another important strengthening effect as demonstrated in previous studies (Wang et al. 2021; Zhou et al. 2016). With an increase in water saturation (20% to 80%), several meniscus effects are observed. However, they will be weakened when the specimen is fully saturated (100%) because the pore water is filled in every crack.

For porous sediments and APRs, the dynamic mechanical behaviors, such as the dynamic compressive strength and fracture process, varies with water saturation. Therefore, the microstructure plays an important role in determining the influence of water saturation on the dynamic mechanical characteristics (Gu et al. 2019). Understanding this relationship is essential for making informed decisions regarding water injection parameters aimed at preventing rock burst disasters and should be regarded as a key factor in engineering design considerations.

## Conclusion

A series of dynamic compressive experiments on APR specimens were conducted to evaluate the influence of water saturation on dynamic mechanical behaviors. The investigation involved a systematic analysis of failure modes, stress–strain curves, dynamic uniaxial compressive strength, critical strain, fragmentation, and energy dissipation.

- (1) The dynamic compressive behavior of the APR was significantly influenced by water saturation. With an increase in water saturation, the dynamic compressive strength of the unsaturated specimens exhibited a noticeable upward trend. Additionally, the wet specimens exhibited a higher propensity for failure, resulting in increased dissipated energy and finer fragments. Moreover, the average fragmentation size and required loading rate for pulverization failure increased significantly. Overall, wet specimens were considerably prone to failure, with higher dissipated energy and finer fragments.
- (2) The loading rate greatly determines the dynamic compressive behavior of the APR with different water saturation levels. On one hand, most mechanical characteristics, such as dynamic uniaxial compressive strength, critical strain, average fragment sizes, and dissipated energies, exhibited a significant rate dependency. On the other hand, certain mechanical behaviors, including the failure modes, dynamic uniaxial compressive strength, and FSDs, exhibited different rate dependencies depending on the water saturation levels under various loading rates.
- (3) The dynamic mechanical behavior of the specimens was influenced by their microstructures, impacting

the effect of water saturation. In the case of APR, the random distribution of microcracks weakened the relationship between certain mechanical properties (failure types, fragmentation types, critical strain, and dissipated energy) and water saturation.

- (4) The effect of water saturation is found to be beneficial in mitigating rock breakage and rock burst disasters. This crucial characteristic should be considered during the design of underground engineering projects.

**Acknowledgements** This work was supported by the National Natural Science Foundation of China (NSFC) under Grants # 52079091 and # 42141010, and the Natural Science Foundation of Tianjin under Grants # 21JCZXC00040.

**Data Availability** The data that support the findings of this study are available from the corresponding author upon reasonable request.

## Declarations

**Competing interests** The authors declare no competing interests.

## References

- Aben FM, Doan ML, Gratier JP, Renard F (2017) High strain rate deformation of porous sandstone and the asymmetry of earthquake damage in shallow fault zones. *Earth Planet Sc Lett* 463:81–91. <https://doi.org/10.1016/j.epsl.2017.01.016>
- Abu Bakar MZ, Gertsch LS (2013) Evaluation of saturation effects on drag pick cutting of a brittle sandstone from full scale linear cutting tests. *Tunn Undergr Sp Tech* 34:124–134. <https://doi.org/10.1016/j.tust.2012.11.009>
- Abu Bakar MZ, Gertsch LS, Rostami J (2014) Evaluation of fragments from disc cutting of dry and saturated sandstone. *Rock Mech Rock Eng* 47:1891–1903. <https://doi.org/10.1007/s00603-013-0482-8>
- Atkinson BK (1982) Subcritical crack propagation in rocks: theory, experimental results and applications. *J Struct Geol* 4:41–56. [https://doi.org/10.1016/0191-8141\(82\)90005-0](https://doi.org/10.1016/0191-8141(82)90005-0)
- Barber T, Griffith WA (2017) Experimental constraints on dynamic fragmentation as a dissipative process during seismic slip. *Philos T R Soc A* 375:20160002. <https://doi.org/10.1098/rsta.2016.0002>
- Cai X, Zhou Z, Du X (2020a) Water-induced variations in dynamic behavior and failure characteristics of sandstone subjected to simulated geo-stress. *Int J Rock Mech Min Sci* 130:104339. <https://doi.org/10.1016/j.ijrmms.2020.104339>
- Cai X, Zhou Z, Zang H, Song Z (2020b) Water saturation effects on dynamic behavior and microstructure damage of sandstone: phenomena and mechanisms. *Eng Geol* 276:105760. <https://doi.org/10.1016/j.enggeo.2020.105760>
- Chen W, Song B (2011) *Split Hopkinson (Kolsky) Bar*. Springer, Boston. <https://doi.org/10.1007/978-1-4419-7982-7>
- Chen W, Song B, Frew DJ, Forrestal MJ (2003) Dynamic small strain measurements of a metal specimen with a split Hopkinson pressure bar. *Exp Mech* 43:20–23. <https://doi.org/10.1007/BF02410479>
- da Silva MR, Schroeder C, Verbrugge J-C (2008) Unsaturated rock mechanics applied to a low-porosity shale. *Eng Geol* 97:42–52. <https://doi.org/10.1016/j.enggeo.2007.12.003>
- Daugherty R, Franzini J (1965) *Fluid Mechanics with Engineering Applications*, 6th edn. McGraw-Hill, 1965

- Davy CA, Skoczylas F, Barnichon JD, Lebon P (2007) Permeability of macro-cracked argillite under confinement: Gas and water testing. *Phys Chem Earth* 32:667–680. <https://doi.org/10.1016/j.pce.2006.02.055>
- Dyke CG, Dobereiner L (1991) Evaluating the strength and deformability of sandstones. *Q J Eng Geol* 24:123–134. [https://doi.org/10.1016/0148-9062\(91\)91187-V](https://doi.org/10.1016/0148-9062(91)91187-V)
- Einstein HH (1996) Tunnelling in difficult ground - Swelling behaviour and identification of swelling rocks. *Rock Mech Rock Eng* 29:113–124. <https://doi.org/10.1007/BF01032649>
- Erguler ZA, Ulusay R (2009) Water-induced variations in mechanical properties of clay-bearing rocks. *Int J Rock Mech Min Sci* 46:355–370. <https://doi.org/10.1016/j.ijrmmms.2008.07.002>
- Gang H (2003) Rock stability under different fluid flow conditions. University of Waterloo
- Gu H, Tao M, Cao W, Zhou J, Li X (2019) Dynamic fracture behaviour and evolution mechanism of soft coal with different porosities and water contents. *Theor Appl Fract Mec* 103:102265. <https://doi.org/10.1016/j.tafmec.2019.102265>
- Gu H, Tao M, Li X, Cao W, Li Q (2021) Dynamic response and meso-deterioration mechanism of water-saturated sandstone under different porosities. *Measurement* 167. <https://doi.org/10.1016/j.measurement.2020.108275>
- Hadizadeh J, Law RD (1991) Water-weakening of sandstone and quartzite deformed at various stress and strain rates. *Int J Rock Mech Min Geomech Abstr* 28:431–439. [https://doi.org/10.1016/0148-9062\(91\)90081-V](https://doi.org/10.1016/0148-9062(91)90081-V)
- Hawkins ABM, McConnell BJ (1992) Sensitivity of sandstone strength and deformability to changes in moisture content. *Q J Eng Geol* 25:115–130. [https://doi.org/10.1016/0148-9062\(93\)90783-A](https://doi.org/10.1016/0148-9062(93)90783-A)
- Hong L, Zhou Z-l, Yin T-b, Liao G-y, Ye Z-y (2009) Energy consumption in rock fragmentation at intermediate strain rate. *J Cent South Univ T* 16:677–682. <https://doi.org/10.1007/s11771-009-0112-5>
- Hu DW, Zhou H, Zhang F, Shao JF (2010) Evolution of poroelastic properties and permeability in damaged sandstone. *Int J Rock Mech Min Sci* 47:962–973. <https://doi.org/10.1016/j.ijrmmms.2010.06.007>
- Huang S, He Y, Liu G, Lu Z, Xin Z (2021) Effect of water content on the mechanical properties and deformation characteristics of the clay-bearing red sandstone. *B Eng Geol Environ* 80:1767–1790. <https://doi.org/10.1007/s10064-020-01994-6>
- Jiang L, Xu Y, Chen B, Wu B (2021) Effect of water content on the mechanical properties of an artificial porous rock. *B Eng Geol Environ* 80:7669–7681. <https://doi.org/10.1007/s10064-021-02402-3>
- Kim E, Changani H (2016) Effect of water saturation and loading rate on the mechanical properties of Red and Buff Sandstones. *Int J Rock Mech Min Sci* 88:23–28. <https://doi.org/10.1016/j.ijrmmms.2016.07.005>
- Kranz RL (1979) Crack growth and development during creep of Barre granite. *Int J Rock Mech Min Geomech Abstr* 16:23–35. [https://doi.org/10.1016/0148-9062\(79\)90772-1](https://doi.org/10.1016/0148-9062(79)90772-1)
- Li M, Liu X (2021) Experimental and numerical investigation of the failure mechanism and permeability evolution of sandstone based on hydro-mechanical coupling. *J Nat Gas Sci Eng* 95:104240. <https://doi.org/10.1016/j.jngse.2021.104240>
- Li XF, Li HB, Zhang QB, Jiang JL, Zhao J (2018) Dynamic fragmentation of rock material: Characteristic size, fragment distribution and pulverization law. *Eng Fract Mech* 199:739–759. <https://doi.org/10.1016/j.engfracmech.2018.06.024>
- Ma L, Wu J, Wang M, Dong L, Wei H (2020) Dynamic compressive properties of dry and saturated coral rocks at high strain rates. *Eng Geol* 272:105615. <https://doi.org/10.1016/j.enggeo.2020.105615>
- Masoumi H, Horne J, Timms W (2017) Establishing empirical relationships for the effects of water content on the mechanical behavior of Gosford sandstone. *Rock Mech Rock Eng* 50:2235–2242. <https://doi.org/10.1007/s00603-017-1243-x>
- Rossi P (1991) A physical phenomenon which can explain the mechanical behaviour of concrete under high strain rates. *Mater Struct* 24:422–424. <https://doi.org/10.1007/bf02472015>
- Sheng M, Tian S, Cheng Z, Ge H (2019) Insights into the influence of fluid imbibition on dynamic mechanics of tight shale. *J Petrol Sci Eng* 173:1031–1036. <https://doi.org/10.1016/j.petrol.2018.10.026>
- Tang S (2018) The effects of water on the strength of black sandstone in a brittle regime. *Eng Geol* 239:167–178. <https://doi.org/10.1016/j.enggeo.2018.03.025>
- Van Eeckhout EM (1976) The mechanisms of strength reduction due to moisture in coal mine shales. *Int J Rock Mech Min Sci & Geom Abstr* 13:61–67. [https://doi.org/10.1016/0148-9062\(76\)90705-1](https://doi.org/10.1016/0148-9062(76)90705-1)
- Vasarhelyi B, Van P (2006) Influence of water content on the strength of rock. *Eng Geol* 84:70–74. <https://doi.org/10.1016/j.enggeo.2005.11.011>
- Wang H, Jin W, Li Q (2009) Saturation effect on dynamic tensile and compressive strength of concrete. *Adv Struct Eng* 12:279–286
- Wang P, Yin T-b, Hu B-w (2020) Dynamic tensile strength and failure mechanisms of thermally treated sandstone under dry and water-saturated conditions. *T Nonfer Metal Soc* 30:2217–2238. [https://doi.org/10.1016/S1003-6326\(20\)65374-2](https://doi.org/10.1016/S1003-6326(20)65374-2)
- Wang S, Xu Y, Xia K, Tong T (2021) Dynamic fragmentation of microwave irradiated rock. *J Rock Mech Geotech* 13:300–310. <https://doi.org/10.1016/j.jrmge.2020.09.003>
- Wasantha PLP, Ranjith PG, Permata G, Bing D (2018) Damage evolution and deformation behaviour of dry and saturated sandstones: insights gleaned from optical measurements. *Measurement* 130:8–17. <https://doi.org/10.1016/j.measurement.2018.07.075>
- Wawersik WR, Fairhurst C (1970) A study of brittle rock fracture in laboratory compression experiments. *Int J Rock Mech Min Geomech Abstr* 7:561–575. [https://doi.org/10.1016/0148-9062\(70\)90007-0](https://doi.org/10.1016/0148-9062(70)90007-0)
- Wong LNY, Maruvanchery V, Liu G (2016) Water effects on rock strength and stiffness degradation. *Acta Geotech* 11:713–737. <https://doi.org/10.1007/s11440-015-0407-7>
- Xia K, Yao W (2015) Dynamic rock tests using split Hopkinson (Kolsky) bar system – A review. *J Rock Mech Geotech* 7:27–59. <https://doi.org/10.1016/j.jrmge.2014.07.008>
- Xia K, Nasser MHB, Mohanty B, Lu F, Chen R, Luo SN (2008) Effects of microstructures on dynamic compression of Barre granite. *Int J Rock Mech Min Sci* 45:879–887. <https://doi.org/10.1016/j.ijrmmms.2007.09.013>
- Xu Y, Yao W, Wang S, Xia K (2020) Investigation of the heat-treatment effect on rock fragmentation characteristics using the dynamic ball compression test. *Rock Mech Rock Eng* 53:2095–2108. <https://doi.org/10.1007/s00603-019-02038-6>
- Xu Y, Yang Y, Li X, Wu B, Yao W (2022) Dynamic compressive test of saturated sandstones under ambient Sub-Zero temperature. *Exp Mech*. <https://doi.org/10.1007/s11340-022-00908-9>
- Zhang Z, Gao F (2015) Experimental investigation on the energy evolution of dry and water-saturated red sandstones. *Int J Min Sci Techno* 25:383–388. <https://doi.org/10.1016/j.ijmst.2015.03.009>
- Zhang QB, Zhao J (2014) A review of dynamic experimental techniques and mechanical behaviour of rock materials. *Rock Mech Rock Eng* 47:1411–1478. <https://doi.org/10.1007/s00603-013-0463-y>
- Zhao Y, Liu S, Jiang Y, Wang K, Huang Y (2016) Dynamic tensile strength of coal under dry and saturated conditions. *Rock Mech Rock Eng* 49:1709–1720
- Zhao K, Yang D, Zeng P, Huang Z, Wu W, Li B, Teng T (2021) Effect of water content on the failure pattern and acoustic emission characteristics of red sandstone. *Int J Rock Mech Min Sci* 142:104709. <https://doi.org/10.1016/j.ijrmmms.2021.104709>
- Zhao G, Li X, Xu Y, Xia K (2022) A modified triaxial split Hopkinson pressure bar (SHPB) system for quantifying the dynamic

- compressive response of porous rocks subjected to coupled hydraulic-mechanical loading. *Geomech Geophys Geo* 8:29. <https://doi.org/10.1007/s40948-021-00335-5>
- Zhou Y et al (2012) Suggested methods for determining the dynamic strength parameters and mode-I fracture toughness of rock materials. *Int J Rock Mech Min Sci* 49:105–112. <https://doi.org/10.1016/j.ijrmms.2011.10.004>
- Zhou Z-l, Cai X, Zhao Y, Chen L, Xiong C, Li X-b (2016) Strength characteristics of dry and saturated rock at different strain rates. *T Nonferr Metal Soc* 26:1919–1925. [https://doi.org/10.1016/S1003-6326\(16\)64314-5](https://doi.org/10.1016/S1003-6326(16)64314-5)
- Zhou Z, Cai X, Ma D, Cao W, Chen L, Zhou J (2018) Effects of water content on fracture and mechanical behavior of sandstone with a low clay mineral content. *Eng Fract Mech* 193:47–65. <https://doi.org/10.1016/j.engfracmech.2018.02.028>
- Zhou Z, Cai X, Ma D, Du X, Chen L, Wang H, Zang H (2019) Water saturation effects on dynamic fracture behavior of sandstone. *Int J Rock Mech Min Sci* 114:46–61. <https://doi.org/10.1016/j.ijrmms.2018.12.014>

Springer Nature or its licensor (e.g. a society or other partner) holds exclusive rights to this article under a publishing agreement with the author(s) or other rightsholder(s); author self-archiving of the accepted manuscript version of this article is solely governed by the terms of such publishing agreement and applicable law.